

Ion and electron acceleration in the field-reversed configuration with an odd-parity rotating magnetic field^{a)}

A. H. Glasser^{b)}

Mail Stop K717, Los Alamos National Laboratory, P.O. Box 1663, Los Alamos, New Mexico 87545

S. A. Cohen

Princeton Plasma Physics Laboratory, P.O. Box 451, Princeton, New Jersey 08543

(Received 1 November 2001; accepted 18 January 2002)

The method for accelerating ions and electrons in the field-reversed configuration using odd-parity rotating magnetic fields (RMFs) in the ion-cyclotron range-of-frequencies (ICRF) is studied. The approach is based on long, accurate numerical integration of Hamilton's equations for single-particle orbits. Rapid ion heating to thermonuclear conditions occurs in <0.1 ms in a modest-sized FRC. Strong variation of the magnetic-field strength over the confinement region prevents a true cyclotron resonance, resulting in stochastic though effective heating. Lyapunov exponents are computed to demonstrate chaotic orbits. Electrons are also effectively heated in this frequency range, primarily by a mechanism involving trapping in the wells of the azimuthal electric field. Odd-parity RMF promotes oppositely directed ion and electron motion near the minor axis, appropriate for supporting the plasma current. © 2002 American Institute of Physics. [DOI: 10.1063/1.1459456]

I. INTRODUCTION

As a fusion reactor, the field-reversed configuration¹ (FRC) has attractive features, notably a linear magnet geometry and high- β operation ($\beta \equiv$ plasma pressure/magnetic field pressure). The latter is essential for burning advanced, aneutronic fuels, which would considerably ease important engineering and environmental problems.² Several physics challenges remain for the FRC to be developed into a practical fusion device: adequate energy confinement, stability against the internal tilt mode,³ and practical methods to sustain the plasma configuration and heat the ions to fusion-relevant temperatures, suitable for the relatively compact FRC.⁴

This paper examines the use of a new class of rotating magnetic fields (RMFs), those of odd parity about the midplane,^{5,6} to accelerate both ions and electrons. Odd-parity modes are studied both because they may improve energy confinement by maintaining field-line closure and because they have a local maximum in the induced azimuthal electric field at the midplane. The latter property is shown to be important to heating.

Even-parity RMFs have been successfully used, particularly in rotamak devices,^{7,8} to make plasma, drive toroidal current, and obtain field reversal. In studies of current drive in rotamaks,⁹ usually only electron motion has been considered because the RMF frequency ω has been chosen to be large compared to the ion-cyclotron frequency in the field of the RMF, and the resulting ion motion was thus therefore assumed to be a mere quiver, not of practical importance. However, ω may be comparable to the ion cyclotron frequency Ω_i in the main confining magnetic field. This results

in effective ion heating across a broad resonance, which we further investigate here for the case of odd parity.⁶

Perhaps it is not surprising that the most effective RMF frequency for accelerating ions is the ion-cyclotron range-of-frequencies (ICRFs).⁶ What is surprising is that this same ICRF frequency range is effective at accelerating electrons, though by a markedly different mechanism, trapping in the wells of the azimuthal electric field. In addition to heating, the odd-parity RMF promotes oppositely directed electron and ion motion near the minor axis, directions that add to the plasma current. Odd-parity current generation is, thus, by a different mechanism than commonly evoked to explain even-parity RMF current drive.

Previous studies of ion motion in RMFs have missed these effects because they were of even parity and in different regimes of frequency and duration. Ion motion in infinitely long¹⁰ and finite length¹¹ FRCs with even-parity $\omega \gg \Omega_i$; RMFs have been analyzed for durations up to 250 gyroperiods. These relatively short-time-scale studies showed no ion heating. In marked contrast, we have examined effects of odd-parity RMFs on ion orbits in a FRC for which $\omega \sim \Omega_i$ and find conditions, for laboratory-scale experiments and reactors, under which ions are explosively heated to energies sufficiently high to be fusion-relevant. For a RMF amplitude of order 10^{-3} of the confining magnetic field, typically more than 1000 gyro-orbits are necessary for appreciable heating. We note, in passing, that stability against the tile mode is improved by energetic ions.^{12,13} Finally, the FRC-RMF geometry we use is fully 3D, not 1- or 2D. This fundamentally affects the types of particle orbits possible.¹⁴

Most previous studies of the FRC are based on fluid theory¹⁵⁻¹⁷ or kinetic¹² simulations. This study is based on long, accurate, numerical integration of full Hamiltonian particle orbits. To evaluate the justification of the single-particle

^{a)}Paper Q11 3, Bull. Am. Phys. Soc. **46**, 247 (2001).

^{b)}Invited speaker. Electronic mail: ahg@lanl.gov

approach, we consider three issues: self-consistency of the equilibrium; collective effects on RMF penetration; and collisions.

The equilibrium used here is that of Solov'ev, based on the assumption of a scalar pressure p with $dp/d\Psi$ constant inside the separatrix and vanishing outside, where Ψ is the poloidal magnetic flux.¹⁸ This may not be consistent with a population of large-orbit ions. Based on the results described herein, we expect that the qualitative features of our results should be insensitive to the detailed equilibrium. Verification by means of a self-consistent equilibrium is beyond the scope of this work. A related question concerns the effects of an electrostatic potential $\varphi(\Psi)$. We have explored the effects of such a field and found that, even for values to ± 10 keV, negligible changes occur in the general features. A potential of this size would cause an $\mathbf{E} \times \mathbf{B}$ drift speed about 0.01 times the RMF speed ωr_s .

Certain theories⁹ predict that the RMF penetration is controlled by the ratio of two dimensionless numbers, γ (the ratio of electron-cyclotron frequency in the RMF field to the electron-ion collision frequency) and λ (the ratio of the separatrix radius to the classical skin depth). When $\gamma/\lambda > 1.2$, good penetration is predicted. For the reference FRC (RFRC) described below $\gamma/\lambda \sim 5$. Recent even-parity experiments¹⁹ have shown a lack of full RMF penetration. Since RMF penetration is a critical issue, it is imperative that both theory and experiment be applied to this problem. To date, no odd-parity RMF/FRC experiments have been performed.

Collisions can be neglected if the ratio of system size r_s to mean-free path λ is small, i.e., $r_s/\lambda < 0.1$. For Coulomb collisions, this corresponds to $\mathcal{E}_m^2/n_i r_s > 10^{-11}$, where r_s is the separatrix radius of the FRC, \mathcal{E}_m is the minimum ion energy, and n_i is the plasma density (CGS units except in energy in eV). At $n_i = 10^{14}$, $\mathcal{E}_m = 100$ for a 10 cm radius device. Since λ scales as \mathcal{E}^2 , rapid acceleration by the RMF will cause collisions to be negligible over a much longer trajectory if this condition is satisfied initially.

The studies described here show that, for many initial positions in phase space, small changes in initial conditions produce rapidly divergent trajectories, the defining characteristic of chaotic dynamics.¹⁴ Computation of Lyapunov exponents confirms, clarifies, and quantifies this observation and provides understanding of the scaling of this property. The development of chaotic orbits is important in enhancing thermalization of the energy supplied by the RMF and to stability.

The remainder of this paper is organized as follows. Section II gives equations governing the fields of the FRC and the RMF and the equations of particle motion and describes the numerical procedure for integrating them. Section III describes the behavior ions in these fields, while Sec. IV describes electrons. Section V discusses the divergence of neighboring orbits and the computation and scaling of Lyapunov exponents. Section VI summarizes and discusses the results.

II. BASIC EQUATIONS

This section presents the equations for the particle orbits, discusses the numerical procedure for integrating them, and gives expressions for the FRC confining field and the RMF.

The Hamiltonian for a nonrelativistic particle in an electromagnetic field is given by²⁰

$$H(q_i, p_i) = [(p_r - eA_r)^2 + (p_z - eA_z)^2 + (p_\phi - e\Psi)^2/r^2]/2m + e\varphi, \quad (1)$$

where $q_i = (r, z, \phi)$ are cylindrical coordinates, $p_i = (p_r, p_z, p_\phi)$ are the corresponding canonical angular momenta, e is the charge on the particle, \mathbf{A} is the vector potential, $\Psi \equiv rA_\phi$, φ is the electrostatic potential, and all units are in SI. Hamilton's equations are given by

$$\dot{q}_i = \frac{\partial H}{\partial p_i}, \quad \dot{p}_i = -\frac{\partial H}{\partial q_i}, \quad (2)$$

where dots denote time derivatives.

Equation (2) constitutes a 6th-order nonlinear system of ordinary differential equations (ODEs). We integrate these equations with a Fortran 90 code RMF, using LSODE,²¹ an adaptive multistep method, typically with a relative tolerance of 10^{-9} .

For the confining FRC field, we use a Solov'ev model,²² for which the scalar plasma pressure $p(\Psi)$ is a linear function of Ψ inside the elliptical separatrix,

$$\Psi = \Psi_0 \left(\frac{r^2}{r_s^2} \right) \left(1 - \frac{r^2}{r_s^2} - \frac{z^2}{z_s^2} \right) \quad \text{for} \quad \frac{r^2}{r_s^2} + \frac{z^2}{z_s^2} < 1, \quad (3)$$

where r_s is the radius of the separatrix on the midplane $z = 0$, z_s is the axial position of the X-point on the axis $r = 0$, and we use $\kappa \equiv z_s/r_s$ to denote the elongation. Outside the separatrix, we use the solution of Zakharov and Shafranov,¹⁸ for which $p(\Psi) = 0$. The magnetic flux Ψ is positive inside the separatrix, negative outside, and vanishes on the separatrix. Figure 1(a) shows contours of constant Ψ . While this model field is not self-consistent with the particle orbits we study, we believe that it gives a good qualitative understanding of the orbitals. More general FRC equilibrium fields could be treated, but we have not done so.

The magnetic field associated with Eq. (3) is given by

$$\mathbf{B} = \nabla \times \mathbf{A} = \nabla \Psi \times \nabla \phi. \quad (4)$$

Figure 1(b) shows contours of constant $|\mathbf{B}|$. It vanishes at the X-points, $r = 0$, $z = \pm z_s$, $\Psi = 0$, and at the O-point, $r = r_o = r_s/\sqrt{2}$, $z = 0$, $\Psi = \Psi_0/4$. Since there is no toroidal magnetic field, the magnetic field strength B itself vanishes at those points. B has a maximum B_a , the axial field at the midpoint $r = z = \Psi = 0$; the constant in Eq. (3) can be expressed as $\Psi_0 = B_a r_s^2/2$.

A particle with sufficiently small Larmor radius remains near a surface of constant Ψ . The field on the midplane is

$$B_r = 0, \quad B_z = \pm \frac{2\Psi_0}{r_s^2} \left(1 - \frac{4\Psi}{\Psi_0} \right)^{1/2}, \quad (5)$$

while the field at the extrema of the flux surface is

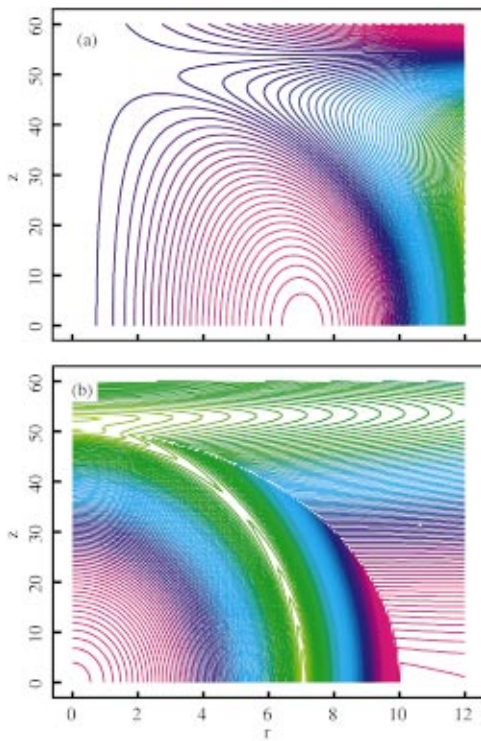


FIG. 1. (Color) Contour plots of FRC model equilibrium, Eqs. (3) and (4). Note different scales for r and z , in cm. (a) Magnetic flux Ψ . (b) Field strength $|\mathbf{B}|$. While $|\mathbf{B}|$ is continuous, its gradient is discontinuous across the separatrix due to the discontinuity in the current there.

$$B_z=0, \quad B_r = \mp \frac{2\Psi_0}{r_s z_s} \left(\frac{\Psi}{\Psi_0} \right)^{1/4} \left[1 - \left(\frac{4\Psi}{\Psi_0} \right)^{1/2} \right]^{1/2}. \quad (6)$$

The ratio of the field strengths at the extrema to that at the midplane is thus

$$R \equiv \frac{B_{\text{mid}}}{B_{\text{ext}}} = \sqrt{2} \kappa \left[1 + \left(\frac{4\Psi}{\Psi_0} \right)^{1/2} \right]^{1/2} \left(\frac{4\Psi}{\Psi_0} \right)^{-1/4}. \quad (7)$$

For a flux surface near the O-point, $\Psi \rightarrow \Psi_0/4$, $R \rightarrow 2\kappa$, while one near the separatrix, $\Psi \rightarrow 0$, $R \rightarrow \infty$. This large variation of field strength has a major effect on the particle orbits, as is shown in Sec. III.

A nonvanishing electrical charge on the plasma may produce an electrostatic potential $\varphi(\Psi)$. We have tested the effects of such a potential and found it to cause small $\mathbf{E} \times \mathbf{B}$ rotation, but not change other interesting features of the orbits. We will not discuss it further.

The vector potential \mathbf{A} for the RMF satisfies the vacuum condition, $\nabla \times (\nabla \times \mathbf{A}) = 0$ and the gauge condition $\nabla \cdot \mathbf{A} = 0$. There are two classes of solution, those whose transverse magnetic fields B_r and B_ϕ have odd and even parity, respectively, about the midplane $z=0$. The odd-parity solutions are given by

$$\mathbf{A} = \{A_r, A_z, A_\phi\} = (2B_0/k) \{I_0(kr) \cos kz \sin \psi, -I_1(kr) \sin kz \sin \psi, I_0(kr) \cos kz \cos \psi\}, \quad (8)$$

where B_0 is the amplitude of the odd-parity RMF, $\psi = \phi - \omega t + \psi_0$ is the phase of the RMF, ω is the RMF angular frequency, and I_0 is a modified Bessel function. We consistently use a right-handed coordinate system in the order given in Eq. (8). For an even-parity RMF, the $\cos kz$ and $\sin kz$ factors are exchanged, the sign of A_z is changed, and the amplitude is denoted B_e . In our computations, we choose $k = \pi/2z_s$, corresponding to 1/2 wavelength between $\pm z_s$.

Previous studies (except those of Cohen *et al.*^{5,6}) have considered only even-parity RMFs. Odd-parity RMFs have two advantages: they avoid opening the magnetic field lines, potentially improving confinement; and they have their peak induced azimuthal electric field at the midplane instead of the X-point, permitting particle acceleration in a magnetic-field-free region. We limit this study to odd-parity RMF.

In the absence of a RMF, the Hamiltonian, Eq. (1), is independent of ϕ and t , and therefore the angular momentum p_ϕ and the energy H are separately conserved. In the presence of a RMF, azimuthal symmetry is lost but H depends on ϕ and t only through $\psi = \theta - \omega t$. It follows²⁰ that the transformed Hamiltonian

$$K \equiv H - \omega p_\phi \quad (9)$$

is conserved, $dK/dt = 0$. K may be interpreted as the energy in the rotating frame of reference.¹¹ We use this conservation law in two ways: by monitoring the relative change in K over a long integration, we verify the precision of our numerical

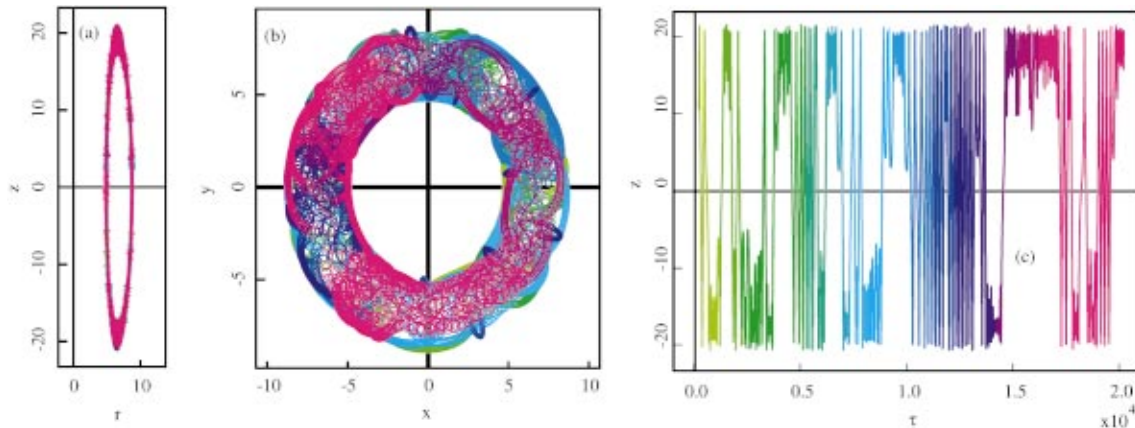


FIG. 2. (Color) Ion orbit without RMF. Spatial dimensions are in cm. Color is used to divide the orbit into 20 distinct time intervals and cross-correlate these intervals among the figures. (a) Projected on the poloidal plane; (b) viewed along z -axis; (c) axial position z vs scaled time τ .

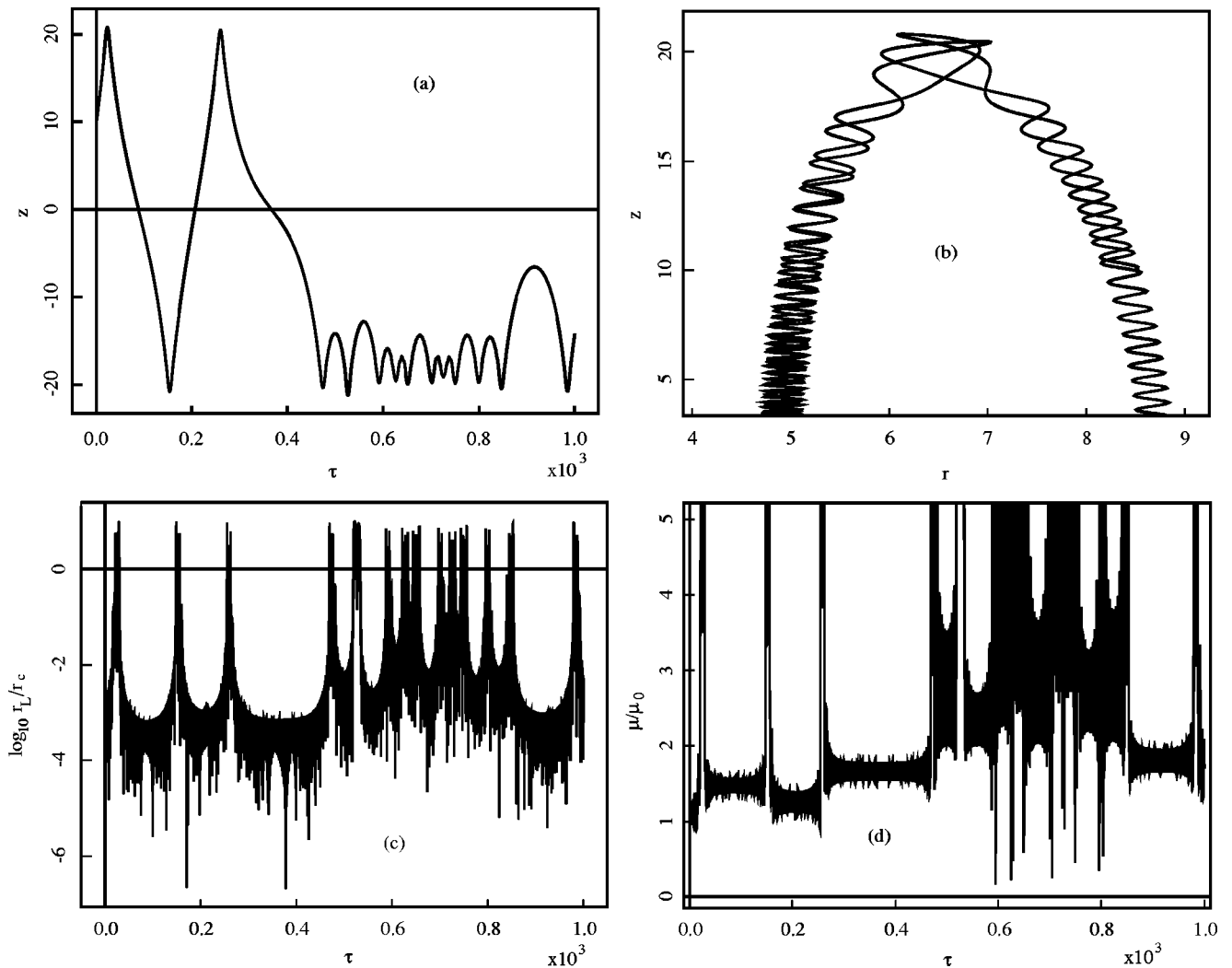


FIG. 3. Ion orbit without RMF, (a) axial position z vs scaled time τ , (b) projected onto poloidal plane; (c) \log_{10} of the ratio of the Larmor radius r_L to the local radius of curvature of the magnetic field line r_c vs scaled time τ ; (d) ratio of magnetic moment μ to its initial value μ_0 vs scaled time τ .

method; and we show in Sec. IV that the inward and outward drift of a particle can be understood in terms of this conservation law.

III. ION ORBITS

In this section we present results for ion orbits, first without and then with odd-parity RMF.

Figure 2 shows an example of deuterium-ion motion in the FRC without RMF. In this and other figures, the FRC has magnetic field strength $B_a = 2$ T, separatrix radius $r_s = 10$ cm, X-point position $z_s = 50$ cm, elongation $\kappa = 5$. The deuteron energy is 100 eV. Color is used to divide the orbit into 20 distinct time intervals and cross-correlate these intervals among the figures. While Fig. 2(a), the orbit projected onto the poloidal (rz) plane, suggests that the orbit circulates regularly around a flux surface, Fig. 2(b), the orbit viewed along the z -axis, shows a more complicated, erratic aspect of the orbit. Figure 2(c) shows axial position z vs scale time $\tau = t/t_0$, normalized to a cyclotron period $t_0 = 2\pi/\Omega_{i0} = 65.6$ ns in the peak magnetic field B_a , with $\Omega_{i0} \equiv q_i B_a/m_i$. It again indicates erratic motion. Over the time interval $\tau = 2$

$\times 10^4$, $t = 1.31$ ms, the relative tolerance used by LSODE is 10^{-9} and the accumulated relative numerical error in the conserved transformed Hamiltonian K is 1.2×10^{-7} .

This erratic behavior can be understood in terms of Speiser collisions,^{23,24} i.e., a breakdown in the conservation of the adiabatic invariant magnetic moment $\mu = mv_{\perp}^2/B$,²⁵ where \mathbf{v}_{\perp} is the particle velocity transverse to the magnetic field. Equation (7) shows that the field strength B drops by more than a factor of $2\kappa = 10$ in going from the midplane to the extrema of the flux surface. Just as the particle rounds the sharp curve in the magnetic field line at its z -extrema, the drop in B causes an increase in the Larmor radius $r_L = v/\Omega_i$, its ratio to the local radius of curvature of the magnetic field line r_c exceeds 1, and conservation of μ is lost. In field-reversed regions, μ is not conserved for much smaller values of r_L/r_c , to 0.03.

Figure 3 shows a closer view of the orbit during the initial time interval, up to $\tau = 10^3$. Figure 3(a) shows the axial motion, indicating that the particle occasionally gets trapped in the magnetic wells at the extrema. Figure 3(b) shows a close-up view of the orbit near the extremum. Far

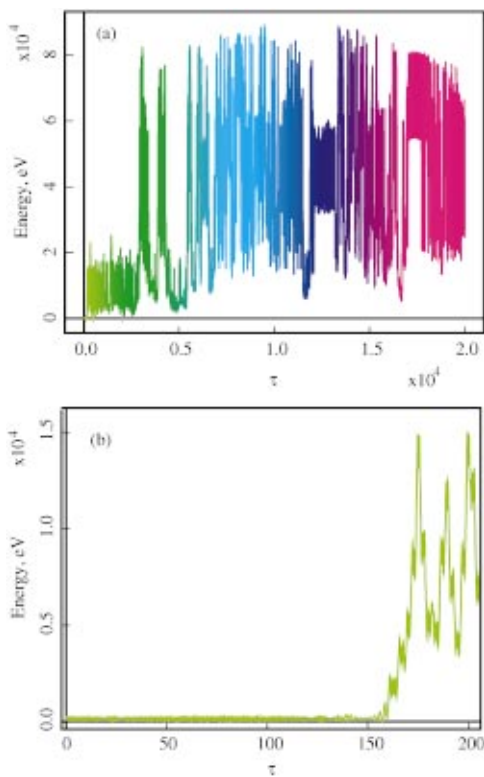


FIG. 4. (Color) Ion orbit with RMF, energy vs scaled time τ . (a) Full run; (b) initial interval.

from the extremum, the Larmor radius is small and the radius of curvature is large, whereas near the extremum the reverse is true. Figure 3(c), $\log_{10} r_L / r_c$ vs τ , shows that the Larmor radius is much less than the radius of local curvature of the magnetic field line far from the extrema, but exceeds it near the extrema. Figure 3(d) shows that the ratio of μ to its initial value is well-conserved between extrema, goes through large jumps near the extrema, and changes by order unity after the jumps. Oscillations in μ about a fixed value are a result dropping higher-order corrections to the asymptotic series for the adiabatic invariant, but secular jumps are significant. The absence of a large, nearly-uniform magnetic field in the FRC, compared to a tokamak, is thus found to make the use of the guiding-center approximation invalid, even for particle energies considerably less than 100 eV.

Figures 4–6 show the orbit of a deuteron with the same initial conditions and duration as the previous one, but with odd-parity RMF applied at $\omega = 7.66 \times 10^7 \text{ s}^{-1} = 80\% \Omega_{i0}$ and amplitude $B_o = 2 \times 10^{-3} \text{ T} = 0.1\% B_a$. Figure 4 shows the important result, that the particle energy rises from its initial 100 eV to 10 keV in a very short time, $\tau = 200$, $t = 13 \mu\text{s}$, to a maximum $> 80 \text{ keV}$, well into the regime of thermonuclear interest, even for advanced, aneutronic fuels. The rate of energy gain is $d\mathcal{E}/dt = q\mathbf{E} \cdot \mathbf{v}$, whose sign and magnitude depend on the relative orientation of the electric field \mathbf{E} and the particle velocity \mathbf{v} . During intervals of rapid energy rise, these vectors remain aligned for a time of order half a cyclotron period. In other time intervals, the energy falls as the deuteron returns energy to the RMF when these vectors are anti-parallel.

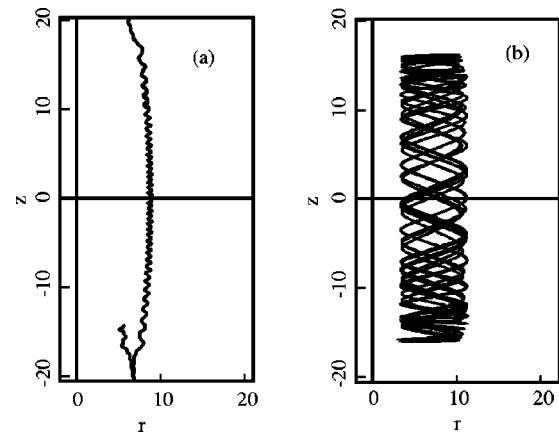


FIG. 5. Ion orbit with RMF, projected onto poloidal plane. (a) Initial time interval; (b) final time interval.

Figures 5 and 6 show the orbit during the first and last time intervals, $0 < \tau < 100$ in green and $19\,900 < \tau < 20\,000$ in magenta. In the initial interval, with energy in the range 50–250 eV, the Larmor radius is very small. In the last interval, with energy in the range 30–60 keV, the Larmor radius is about $r_s/3$. In spite of the large excursions, the particle does not escape confinement. The large Larmor radius orbits are betatron type rather than cyclotron. Betatron orbits may be effective at stabilizing the tilt mode.^{12,13} For numerical runs with the same initial conditions but 10 times longer durations, the maximum energy attained, \mathcal{E}_M , does not increase. However, if the deuteron is initiated with an energy above \mathcal{E}_M , say 100 keV with all other conditions unchanged, the particle energy does not (or rarely) fall below \mathcal{E}_M . As shown later, \mathcal{E}_M depends on the strength of the RMF field, the separatrix radius, and the main field strength.⁶

To elucidate the mechanisms of ion acceleration by the odd-parity RMF, Fig. 7 shows scatter plots of the rate of ion energy gain transverse and parallel to the local magnetic field, as a function of the axial position z and the ratio of the local ion-cyclotron frequency Ω_i to the RMF frequency ω .

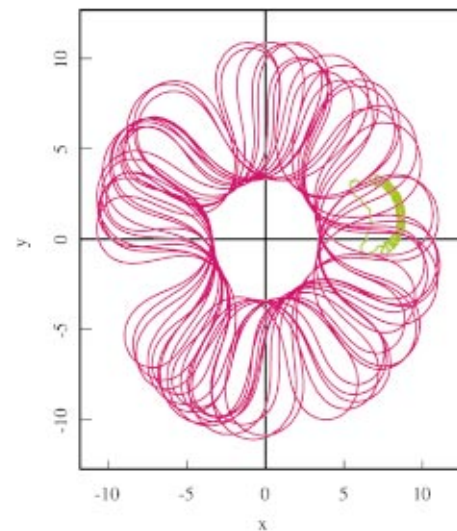


FIG. 6. (Color) Ion orbit with RMF, viewed along the z -axis.

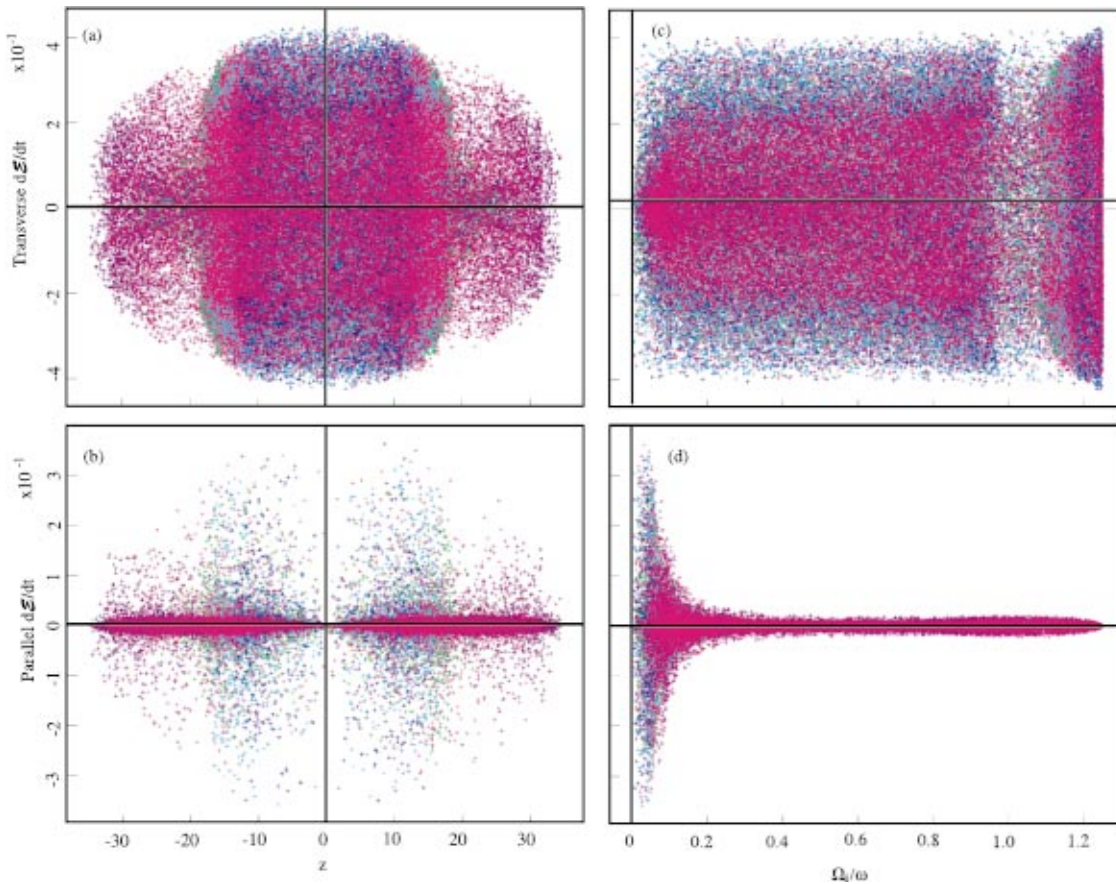


FIG. 7. (Color) Scatter plots of transverse and parallel energy gain. (a) Transverse $d\mathcal{E}/dt$ vs axial position z ; (b) parallel $d\mathcal{E}/dt$ vs axial position z ; (c) transverse $d\mathcal{E}/dt$ vs Ω_i/ω ; (d) parallel $d\mathcal{E}/dt$ vs Ω_i/ω .

While these plots show points along a single orbit, the points are not connected by continuous lines, but are intended to show the correlation between the variables on the abscissa and the ordinate. The induced electric field which accelerates the ions is $\mathbf{E} = -\partial\mathbf{A}/\partial t$, with \mathbf{A} given by Eq. (8). The concentration of $d\mathcal{E}/dt$ at a small z , ± 15 cm, seen in Fig. 7(a), is a consequence of the $\cos kz$ factors in A_r and A_ϕ . This localization of heated ions near the mid-plane is an attractive property of odd-parity RMF. By contrast, the parallel $d\mathcal{E}/dt$ is seen in Fig. 7(b) has a peak away from $z=0$, though not as far as predicted by the $\sin kz$ factor in A_z .

Figures 7(c) and 7(d) show the dependence of the transverse and parallel $d\mathcal{E}/dt$ on the Ω_i/ω . The transverse term is nearly uniform from 0.1 to 1. There is a second, less wide band from 1.1 to 1.25. The 1.25 value corresponds to the two intersections of the separatrix with the midplane, at $r=0$ and r_s and $z=0$; the mechanism for this is not well understood. By contrast, the parallel $d\mathcal{E}/dt$ is peaked at very low values of Ω_i/ω but vanishes at 0, where the z component of the electric field vanishes. The peak at 0.04 is of order the axial bounce frequency.

Figure 8 shows the maximum energy achieved by deuterium ions in 903 runs of the RMF code with different values of the amplitude B_o and the ratio ω/Ω_{i0} . Maximum heating is achieved for ω/Ω_{i0} in a band of order unity about the origin, confirming that the heating mechanism is strongly influenced by ion-cyclotron resonance. The gap very near the

origin is due to the proportionality of the accelerating electric field to ω . Increasing the RMF amplitude raises and broadens the whole curve. The erratic behavior of the curves is further evidence of the stochastic behavior of the orbits.

IV. ELECTRON ORBITS

We have seen in Sec. III that a RMF in the ICRF is very effective at heating ions to thermonuclear temperatures. We see in this section that a RMF at the same frequency can also heat electrons and drive current, by a markedly different mechanism.

Figure 9 shows the behavior of an electron acted on by an odd-parity RMF. The initial position is on the midplane, $z=0$, with the initial radius 2% beyond the O-point, and the initial energy is 100 eV. The RMF has a frequency $\omega = 2 \times 10^{-4} \Omega_{e0} = 0.73 \Omega_{i0} = -7 \times 10^7 \text{ s}^{-1}$, in the ICRF. Figure 9(a) shows energy vs scaled time $\tau = t/t_0$, normalized to an electron-cyclotron period $t_0 = 2\pi/\Omega_{e0} = 17.9$ ps in the peak magnetic field B_a , with $\Omega_{e0} \equiv q_e B_a/m_e$. It shows a sequence of periodic spikes to a maximum energy of 8 keV, with a baseline moving erratically up to a maximum of 5 keV. Figure 9(b) shows the azimuthal angle ϕ in radians vs scaled time τ . It shows a uniform angular velocity within 1% of the RMF frequency, with a small stair-step motion superimposed on it. This constitutes a current which can be used to sustain the FRC.

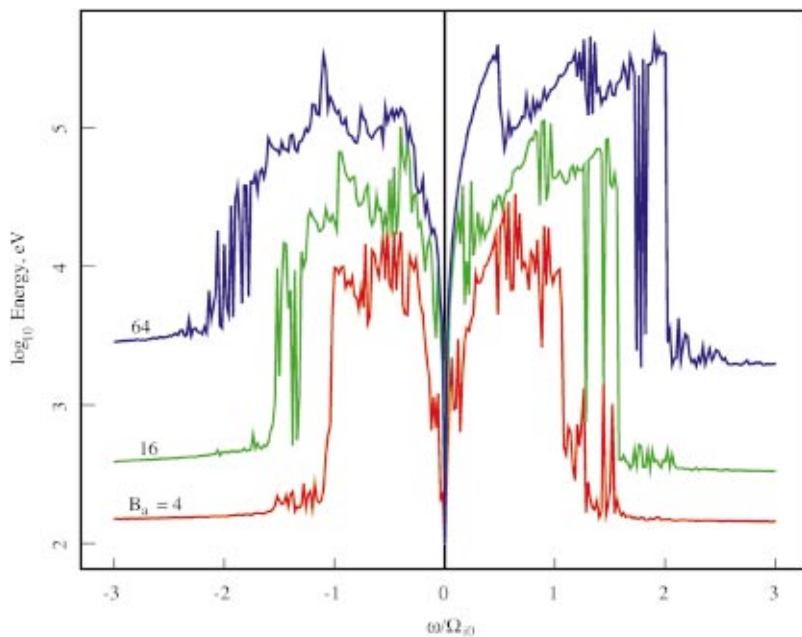


FIG. 8. (Color) \log_{10} maximum energy vs ω/Ω_{i0} for three values of RMF amplitude B_z .

The mechanism responsible for this behavior can be understood in more detail from Fig. 10, showing the time interval $2 \times 10^4 < \tau < 3 \times 10^4$. The peaks of the energy spikes in Fig. 10(a) are correlated with the rapid motion in ϕ , the riser parts in the stairsteps, in Fig. 10(b). For this set of initial conditions, the time between successive spikes is approximately half the period of the RMF. The change in azimuthal angle between successive spikes is approximately $-\pi$. (Other sets of initial conditions will result in smaller or larger steps in ϕ with commensurately smaller or larger times between steps.) The kinetic energy is found to be due almost

entirely to this azimuthal component of the motion, with the radial and axial energies much smaller. When the mean electron v_ϕ is synchronous with the RMF rotation, the electron is trapped in the well formed by the azimuthal electric field, $E_\phi = -\partial A_\phi / \partial t \propto -\cos \psi$. The spikes are due to moving in one direction in the well. Overall, the betatron nature of these near-O-point orbits is responsible for the ratchetlike (unidirectional) behavior of the electron's azimuthal motion. The baseline energy is the kinetic energy when the electron has moved away from the O-point null line and is undergoing Speiser collisions at the field-line z extrema. During that period, the electron stays at nearly constant ϕ until the process begins again. We note that electrons may be heated near the field-line extrema by both the z and r components of \mathbf{E} , in conjunction with the effective Speiser resistivity.

Figure 10(c) further clarifies the picture. It shows the orbit in the plane perpendicular to the z -axis, in the frame rotating with the angular frequency of the RMF. The electron is seen to be trapped in the well of the wave. The spikes in the energy occur when the electron accelerates in the well, moving in the clockwise direction in Fig. 10(c). ϕ is at a maximum at $x=0$. After moving $\sim \pi$ radians clockwise, the electron moves in the counterclockwise direction during its stay near the field-line extrema. The kinetic energy of the particle in this non-inertial frame of reference is K , up to an unspecified constant. If this kinetic energy is sufficiently small, the electron is trapped in the rotating frame of reference, while if it is too large, it can escape the well and rotate. Conservation of K implies that, for $\omega > 0$, electrons move toward the O-point if they gain energy. Electrons exactly in phase with the RMF do not display a step-riser pattern vs ϕ . They also do not display prominent energy spikes.

Electrons near the trapping boundary can be trapped by Speiser collisions. When they are too far from this boundary, as when they are initialized too far from the O-point, they remain passing in the rotating frame.

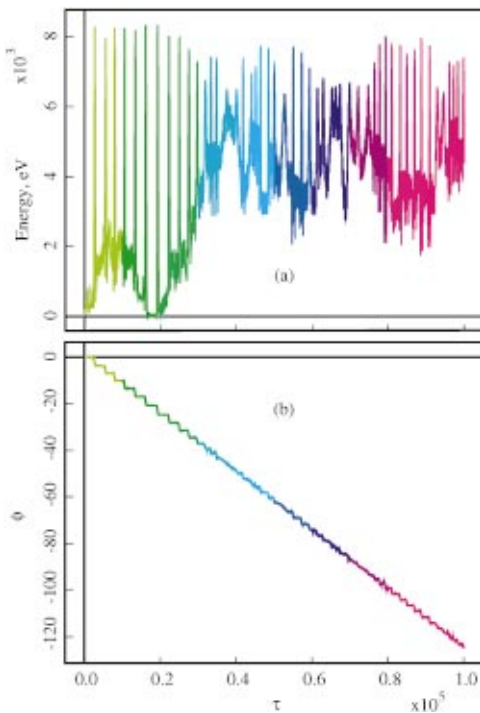


FIG. 9. (Color) Electron orbit with RMF. (a) Energy in eV vs scaled time τ , (b) azimuthal position ϕ in radians vs scaled time τ .

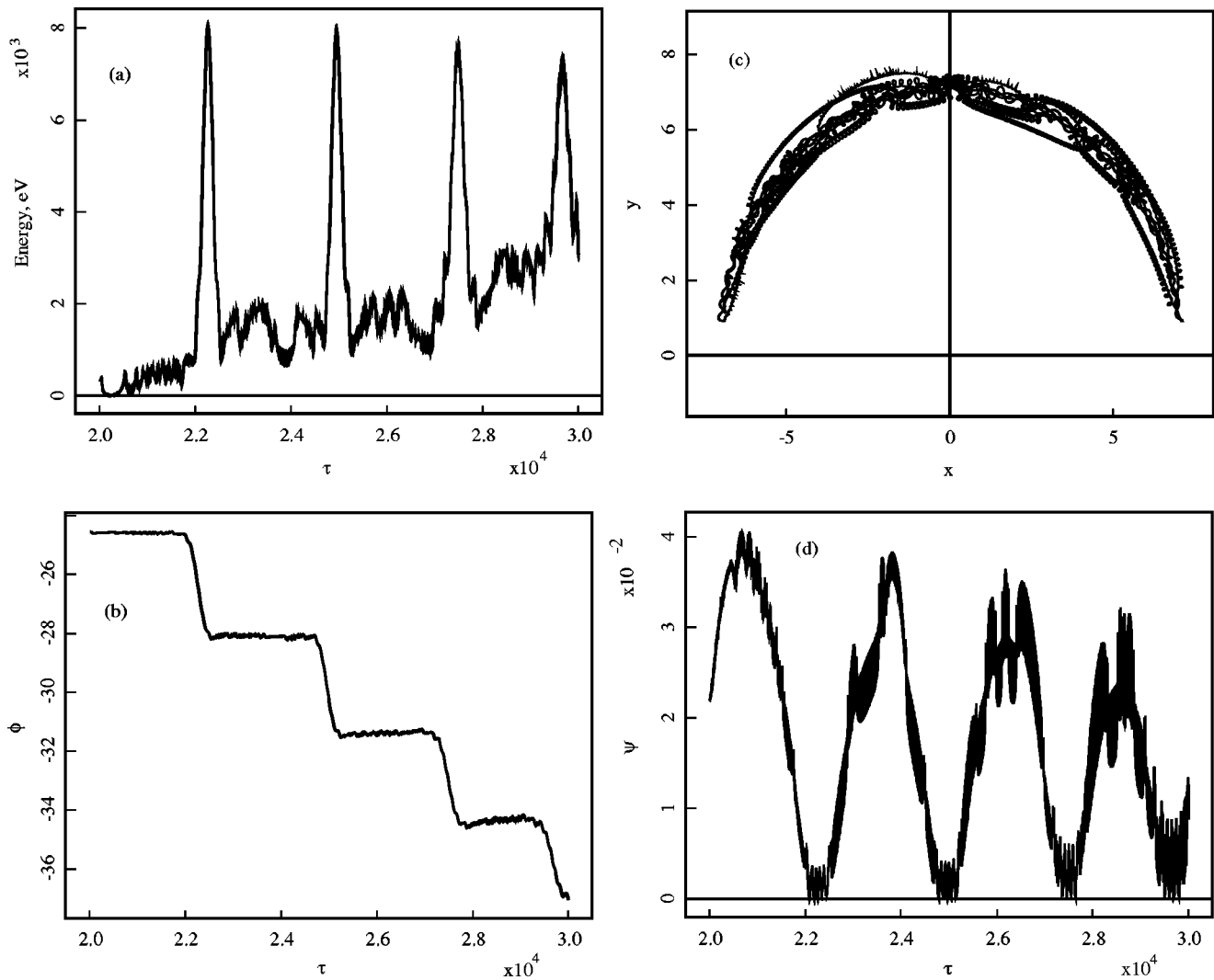


FIG. 10. Electron orbit with RMF (a) energy in eV vs scaled time τ ; (b) azimuthal position ϕ in radians vs scaled time τ ; (c) orbit in frame rotating with the RMF; (d) flux surface label ψ vs scaled time τ .

Figure 10(d) shows one more feature of the motion, the normalized flux surface label $\bar{\Psi} = 1 - 4\Psi/\Psi_0$, with Ψ the FRC toroidal flux, Eq. (3). $\bar{\Psi}$ normalized such that $\bar{\Psi} = 0$ at the O-point and $\bar{\Psi} = 1$ on the separatrix. Figure 10(d) shows that the particle remains everywhere fairly close to the O-point and gets extremely close to it during the energy spikes. This behavior can be understood in terms of the conserved transformed Hamiltonian K , Eq. (9). The angular momentum $p_\phi = mr^2\dot{\phi} - q\Psi$ is dominated by the second term when the Larmor radius is small, so $K \approx H + \omega q\Psi$. Depending on the sign of ω , an increase in the energy H must be balanced by either a decrease or increase of ψ in order to conserve K , resulting in an inward or outward drift.

Figure 11(a) shows the maximum energy achieved by electrons in multiple runs of the RMF code with different values of the amplitude B_o and the ratio of the initial radial position r to the O-point radius r_o . Maximum heating is achieved when the electron is initially near the O-point, with the effective-heating distance from the O-point increasing with RMF amplitude. Figure 11(b) shows the ratio of the total change in the electron's azimuthal angle, $\Delta\phi$, to the

total change in the RMF phase ωt , a value of 1 being indicative of trapping. Both of these figures show that increasing RMF amplitude increases the ability of the electric field to trap the electron.

V. ORBITAL CHAOS

The orbits of particles in the FRC are found to be chaotic, even without RMF. By definition, chaos means that orbits with very close initial conditions diverge from each other exponentially.¹⁴ This behavior is illustrated in Fig. 12, showing two 100-eV ion orbits without RMF in red and blue, respectively, with initial radial position $r(t=0)$ differing by one part in 10^5 and all other initial conditions identical. During the initial interval $0 < \tau < 150$, only one orbit is visible, but then they diverge rapidly. Note that this interval is much smaller than those used in the previous figures.

The rate at which nearby orbits diverge can be quantified by means of Lyapunov exponents.^{14,26} Hamilton's equations, Eq. (2), can be expressed compactly as

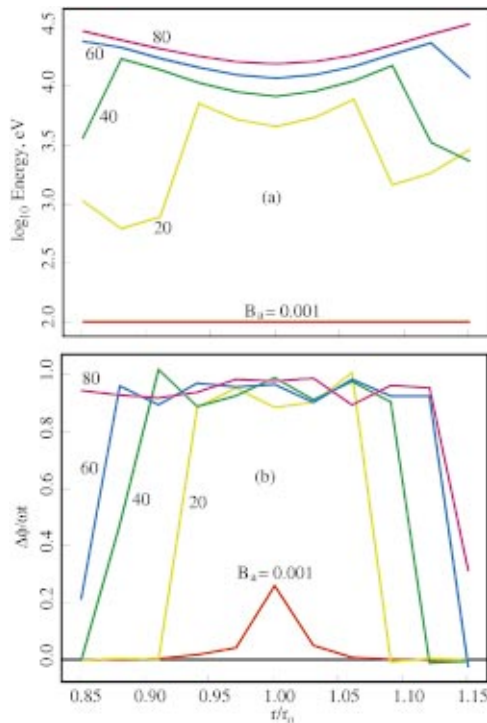


FIG. 11. (Color) Scans of electron behavior over values of initial r/r_0 for several values of the RMS amplitude B_0 . (a) Maximum electron energy; (b) ratio of electron azimuthal angle change $\Delta\phi$ to RMF azimuthal angle change ωt .

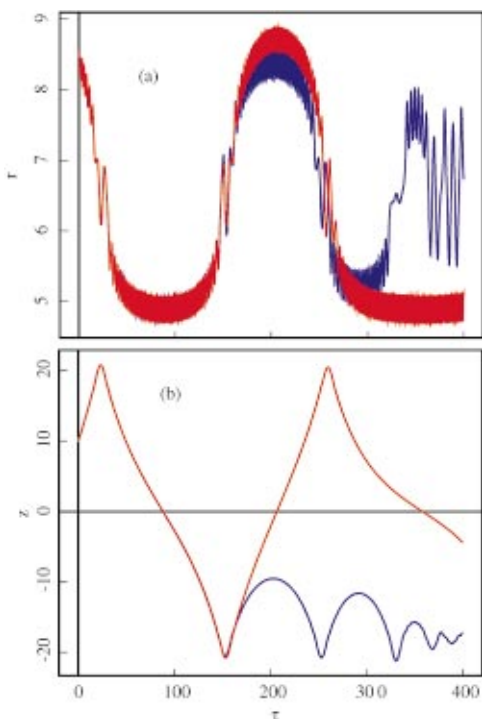


FIG. 12. (Color) Two ions orbit without RMF. With initial radius differing by 1 part in 10^5 . (a) Radial position r vs scaled time τ , (b) axial position z vs scaled time τ .

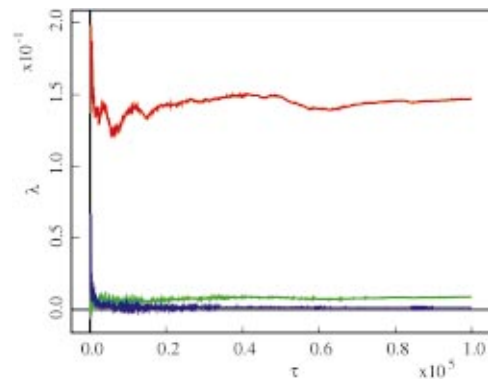


FIG. 13. (Color) Ion orbit without RMF, Lyapunov exponents λ vs scaled time τ .

$$\dot{\mathbf{z}} = \mathbf{J} \frac{\partial H}{\partial \mathbf{z}}, \quad (10)$$

in terms of the phase-space position column-vector $\mathbf{z} \equiv \{r, z, \phi, p_r, p_z, p_\phi\}^T$ and the unit symplectic matrix $\mathbf{J} = \{\{\mathbf{0}, \mathbf{1}\}, \{-\mathbf{1}, \mathbf{0}\}\}$. Denote a nearby trajectory by $\mathbf{z} + \delta\mathbf{z}$, with $|\delta\mathbf{z}| \ll |\mathbf{z}|$. Equation (10) is linearized about the fiducial trajectory \mathbf{z} ,

$$\delta\dot{\mathbf{z}} = \mathbf{L} \delta\mathbf{z}, \quad \mathbf{L} \equiv \mathbf{J} \frac{\partial^2 H}{\partial \mathbf{z} \partial \mathbf{z}}. \quad (11)$$

It is easily seen that L is Hamiltonian, defined by the prop-

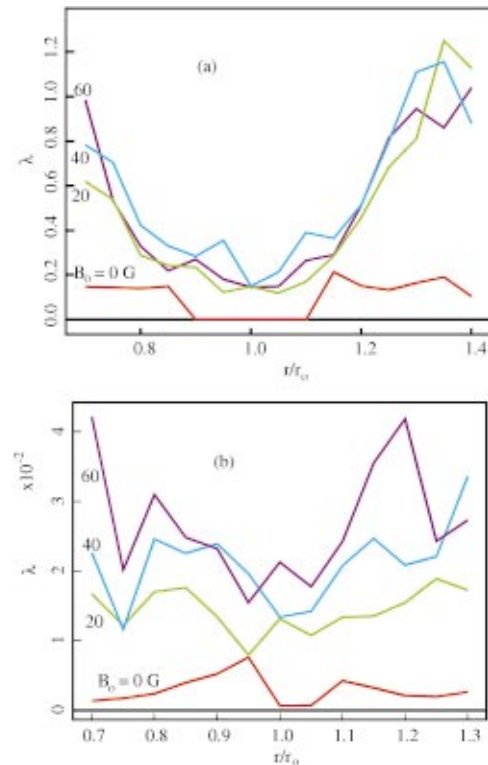


FIG. 14. (Color) Largest Lyapunov exponent λ vs initial r/r_0 for several values of the RMF amplitude B_0 . (a) Ions; (b) electrons.

erty $\mathbf{JLJ}=\mathbf{L}^T$. Let U denote a square matrix whose column vectors are six independent solutions of Eq. (11). Then U satisfies a matrix form of Eq. (11),

$$\dot{\mathbf{U}}=\mathbf{L}\mathbf{U}. \quad (12)$$

If the initial conditions are chosen such that $\mathbf{U}^T\mathbf{J}\mathbf{U}=\mathbf{J}$, then this property is preserved because of the Hamiltonian property of L . Such a matrix of solutions is called symplectic.

Independent column vector solutions to Eq. (12) have the asymptotic form,

$$\lim_{\tau \rightarrow \infty} \mathbf{u}_i(\tau) = \mathbf{u}_{i0}(\tau) e^{\lambda_i \tau}, \quad (13)$$

with six independent real solutions for the eigenvalues λ_i , the Lyapunov exponents, and corresponding bounded eigenvectors $\mathbf{u}_{i0}(t)$, and with the time behavior expressed in terms of the normalized time τ used previously. This can be solved for the Lyapunov exponents,

$$\lambda_i = \lim_{\tau \rightarrow \infty} \frac{\ln |\mathbf{u}_i(\tau)|}{\tau}. \quad (14)$$

For the symplectic solutions to Eq. (12), the Lyapunov exponents come in pairs of equal magnitude and opposite sign, so only the positive Lyapunov exponents need to be computed. Various methods exist for numerically separating the smaller positive Lyapunov exponents from the larger ones, of which the most efficient is occasional Gram–Schmidt re-orthogonalization.²⁶

Figure 13 shows the result of such a computation for the same orbit as in Fig. 12. Convergence is slow but recognizable. The three final values for the Lyapunov exponents are 1.5×10^{-1} , 9.2×10^{-3} , and 1.4×10^{-3} . The effect of the RMF is found to increase the magnitudes of the Lyapunov exponents.

The divergence of the solutions in Fig. 12 by $\tau=150$ is understandable in terms of this exponential growth. It should be understood that the actual magnitudes of the Lyapunov exponents constitute a long-time average measure of the divergent tendencies and may not accurately represent the short-term behavior shown in Fig. 12.

Figure 14 shows the behavior of the largest Lyapunov exponent λ for 52 cases of ion and electron orbits for a range of values of r/r_o and B_o . For ions with RMF, λ nearly vanishes near the O-point, and generally increases with RMF amplitude and distance from the O-point. There is a similar trend, though not so clear, for the electrons. Since the definition of λ in Eq. (14) uses the scaled time τ for each species, and the ratio in the magnitude between ions and electrons is approximately proportional to the square root of the mass ratio, the rate of separation of nearby orbits is clearly related to the thermal velocity of the particle, which also explains the increase with RMF amplitude.

There are several implications of these results. Computation of any particular orbit is extremely sensitive, not only to initial conditions, but to small changes in numerical toler-

ance and even differences in the details of floating point methods between different computers. Physically, the different trajectories of many nearby particles should contribute to thermalization and diffusion of the particle distribution function.

VI. DISCUSSION

We have presented results of long-time, highly-accurate numerical integration of individual particle orbits in the FRC with an odd-parity RMF in the ICRF. These results may be regarded as complementary to other treatments of the FRC based on fluid, particle-in-cell, and kinetic approaches. They show that the odd-parity RMF may provide an effective method to heat ions to thermonuclear conditions, including for advanced, aneutronic fuel cycles, while leaving them well-confined. The resulting large-orbit ions may be effective in stabilizing the FRC against the tilt instability. The RMF is also effective at heating and driving current in the electrons. These conclusions should warrant new experimental investigations and further theoretical investigations.

ACKNOWLEDGMENTS

The authors would like to thank John Finn for many helpful discussions and Tom Kornack for extensive help in preparing the manuscript.

This work is supported by U.S. Department of Energy Contracts Nos. W-7405-ENG-36 and DE-AC02-76-CHO-3073.

¹M. Tuszewski, Nucl. Fusion **28**, 2033 (1988).

²D. Barnes, M. Binderbauer, R. B. Brooks *et al.*, Fusion Technol. **30**, 116 (1996).

³M. Rosenbluth and M. Bussac, Nucl. Fusion **19**, 489 (1979).

⁴N. Rostoker, M. Binderbauer, and H. Monkhorst, Science **278**, 1419 (1997).

⁵S. A. Cohen and R. Milroy, Phys. Plasmas **7**, 2539 (2000).

⁶S. A. Cohen and A. H. Glasser, Phys. Rev. Lett. **85**, 5114 (2000).

⁷H. Blevin and P. Thonemann, Nucl. Fusion Suppl. Part 1, 55 (1962).

⁸I. Jones, Phys. Plasmas **6**, 1950 (1999).

⁹R. Milroy, Phys. Plasmas **6**, 2771 (1999).

¹⁰W. Hugrass and I. Jones, J. Plasma Phys. **29**, 155 (1983).

¹¹W. Hugrass and M. Turley, J. Plasma Phys. **37**, 1 (1987).

¹²D. Barnes, J. Schwarzmeier, H. Lewis, and C. Seyler, Phys. Fluids **29**, 2616 (1986).

¹³L. Steinhauer and A. Ishida, Phys. Fluids B **2**, 2422 (1990).

¹⁴A. Lichtenberg and M. Leiberman, *Regular and Chaotic Dynamics* (Springer-Verlag, New York, 1992).

¹⁵R. Milroy and J. Brackbill, Phys. Fluids **25**, 775 (1982).

¹⁶R. Milroy, D. Barnes, R. Bishop, and R. Webster, Phys. Fluids B **1**, 1225 (1989).

¹⁷R. Milroy, Phys. Plasmas **7**, 4135 (2000).

¹⁸L. Zakharov and V. Shafranov, in *Plasma Physics*, edited by M. Leontovitch (Consultants Bureau, New York, 1986), Vol. 11, pp. 206–211.

¹⁹J. Slough and K. E. Miller, Phys. Plasmas **7**, 1945 (2000).

²⁰H. Goldstein, *Classical Mechanics* (Addison–Wesley, Reading, 1980).

²¹A. Hindmarsh, in *Scientific Computing*, edited by R. Stepleman (North–Holland, Amsterdam, 1983).

²²L. Solov'ev, Rev. Plasma Phys. **6**, 239 (1976).

²³T. Speiser, J. Geophys. Res. **70**, 4219 (1965).

²⁴J. Chen, J. Geophys. Res., [Space Phys.] **97**, 15011 (1992).

²⁵R. Cohen, G. Rowlands, and J. Foote, Phys. Fluids **21**, 627 (1978).

²⁶K. Ramasubramanian and M. Sriram, Phys. Rev. E **62**, 4850 (2000).